Endosomal escape of delivered mRNA from endosomal recycling tubules visualized at the nanoscale

Prasath Paramasivam[1,8], Christian Franke[1,7,8], Martin Stöter[1], Andreas Höijer[2], Stefano Bartesaghi[3], Alan Sabirsh[2], Lennart Lindfors[2], Marianna Yanez Arteta[2], Anders Dahlén[4], Annette Bak[5], Shalini Andersson[6], Yannis Kalaidzidis[1], Marc Bickle[1] and Marino Zerial[1*]

1. Max Planck Institute of Molecular Cell Biology and Genetics, Pfotenhauerstrasse 108 01307. Dresden, Germany.
2. Advanced Drug Delivery, Pharmaceutical Science R&D, AstraZeneca, Gothenburg, Sweden.
3. Bioscience Metabolism, Research and Early Development Cardiovascular, Renal and Metabolism, BioPharmaceuticals R&D, AstraZeneca, Gothenburg, Sweden.
4. Discovery Sciences R&D, AstraZeneca, Gothenburg, Sweden.
5. Advanced Drug Delivery, Pharmaceutical Science R&D, AstraZeneca, Boston, USA.
6. Medicinal Chemistry, Research and Early Development, Cardiovascular, Renal and Metabolism (CVRM), BioPharmaceuticals R&D, AstraZeneca, Gothenburg, Sweden.
7. Current address: Institute of Applied Optics and Biophysics, Friedrich-Schiller-University Jena, Max-Wien Platz 4, 07743 Jena, Germany
8. Equal contribution

***** Correspondence: Marino Zerial (zerial@mpi-cbg.de).

Abstract

Delivery of exogenous mRNA using lipid nanoparticles (LNP) is a promising strategy for therapeutics. However, a bottleneck remains the poor understanding of the endosomal parameters that correlate with endosomal escape vs. cytotoxicity. To address this problem, we compared the endosomal distribution of six LNP-mRNA formulations of diverse chemical composition and efficacy in primary human adipocytes. Quantitative multi-parametric microscopic analysis revealed that total LNP uptake is a poor predictor of delivery. Prolonged uptake impaired endosomal acidification causing mRNA accumulation in compartments defective in cargo transport and unproductive for delivery, indicating parameters of cytotoxicity. In contrast, early endocytic/recycling compartments have the highest probability for mRNA escape. By super-resolution microscopy we could resolve single fluorescently labelled mRNA within sub-endosomal compartments and capture events of mRNA escape from Transferrin-positive recycling tubules. Our results shed light into the mechanisms of endosomal escape and define quantitative parameters that can guide the development of mRNA formulations towards high efficacy and low cytotoxicity.

Introduction

In recent years, RNAs have emerged as potentially powerful therapeutics to modify or deliver genetic information[1]. RNAs can be exploited to inhibit gene expression (splicing modulators, siRNAs and antisense oligonucleotides), express proteins (mRNA) or gene editing (CRISPR/Cas9 system). An increasing number of RNA-based therapeutics have been developed, and some have proven effective for clinical treatment[2-4]. More recently, optimization of chemical and physical properties have focused the attention on mRNA-based therapeutics, including for vaccines[5, 6]. Nevertheless, although the clinical application of mRNA has benefited from chemical modifications that increased stability and reduced immunogenicity, efficacy remains a challenge due to limited or poor delivery[7].

Lipid nanoparticles (LNP) are currently the non-viral RNA delivery platform of choice[7, 8]. LNP have different chemical compositions and show vastly different nucleic acid delivery efficiency, toxicity and immunological liability. The mechanistic basis for such differences is unclear. Since delivery is a multi-step process[9], attempting structure/activity relation without understanding the underlying mechanisms can yield complex and contradicting results, as the outcome of experiments is influenced by the non-linear combination of the various steps. Besides endocytosis, a major challenge remains the ability of exogenously delivered mRNA to cross the endosomal membrane and gain access to the site of function, the cytoplasm or the nucleus[10]. Ineffective escape from endosomes imposes higher dosage, thus contributing to toxicity. Toxicity is due to both cell autonomous, i.e. cytotoxicity, as well non-cell autonomous effects, e.g. inflammation[8, 11]. The reasons for cytotoxicity are diverse and include oxidative stress and induction of apoptosis[12]. However, whether and how cytotoxicity implicates alterations of the endosomal system is unknown. The precise physico-chemical mechanisms whereby LNP help mRNA escape from the endosomal lumen remain unclear, hindering the development of delivery platforms following rational design-based chemical synthesis. Escape efficiency arguably depends on the distribution of LNP in various subcellular compartments, of which only a select few are poised to macromolecule escape. Therefore, understanding the mechanisms of endosomal escape is essential to enable design strategies tailored to improve this specific step. Here, we addressed this problem by a systematic comparison of uptake, endosomal distribution and effects on the endocytic system of six mRNA-containing LNP with varying efficacy and toxicity in primary human adipocytes, to identify candidate parameters diagnostic for the efficacy of delivery.

Results:

LNP-mRNA internalization is necessary but not sufficient to predict delivery efficacy

We aimed to determine whether differences in LNP-mediated mRNA (LNP-mRNA) delivery efficacy may originate from variations in 1) uptake and/or 2) intracellular trafficking to endocytic compartments with higher probability to escape than others. To this end, we performed a comparative analysis on uptake and endosomal distribution of mRNA encoding eGFP formulated in six distinct LNP with similar size distribution (54-73 nm) and mRNA content (Supplementary Table 1) but chosen on the basis of various chemical structures of the cationic lipid (Extended Data Fig. 1a), efficacy, as evaluated by intensity of eGFP expression (Fig. 1a, Extended Data Fig. 2a) as well as toxicity (Ex. MC3 Vs MOD5 or L319)[13, 14]. We used primary human adipocytes, as a relevant cell model for mRNA administered by subcutaneous injection and detected the mRNA with single molecule fluorescence in situ hybridization (smFISH), unless otherwise mentioned. Measurement of uptake kinetics indeed showed that internalization and trafficking vary between the LNP-mRNA (Fig. 1b). Interestingly, although in most cases uptake correlated with transfection efficacy (e.g. MC3 vs. L319), L608 demonstrated highest eGFP expression despite moderate LNP-mRNA uptake compared with e.g. MC3 and ACU5 (Fig. 1b). These results suggest that, besides uptake efficiency, the LNP may deliver mRNA with diverse efficacy because they differ qualitatively and/or quantitatively in endosomal distributions.

Internalized cargo molecules are transported to early endosomes where they are either sorted to recycling endosomes and returned to the plasma membrane, or to late endosomes/lysosomes where they are degraded. For LNP to be effective and non-toxic, they should carry mRNA to compartments where it can be released into the cytoplasm or at least degraded without interfering with endosomal function. Therefore, the average residence time of LNP-mRNA in compartments that are favourable for escape must be rate-limiting for delivery[15]. Such residence time is proportional to the accumulation of LNP-mRNA. To gain insights into these properties, we measured the distribution of endocytosed mRNA in endosomal compartments immuno-stained against EEA1 and APPL1 to label early endosomes[16], Rab11 for recycling endosomes and LAMP1 for late endosomes/lysosomes (Fig. 1c-f). Interestingly, we found that the proportion of LNP-mRNA differed quantitatively between compartments. First, LNP-mRNA distribution in EEA1 early endosomes is significantly higher than other compartments (Fig. 1g, compare Y-axis). Second, the fraction of LNP-mRNA in early (EEA1, APPL1) and recycling (Rab11) endosomes is higher for the more efficient LNP (L608, MC3 and ACU5) compared to the less efficient LNP (ACU22, MOD5 and L319). This tendency was not apparent in LAMP1 endosomes (compare L608 with MC3 and ACU5), suggesting that this compartment may contribute minimally to mRNA delivery.

Accumulation of mRNA in Rab11 endosomes is a strong predictor of delivery efficacy

In order to identify the compartment(s) with the highest probability of escape, we used a directed acyclic graph (DAG), a general mathematical tool to infer dependencies between observed variables by differential correlation (Extended Data Fig. 3a, **see Methods**). We applied DAG to the sequential transport of LNP-mRNA through the compartments of the endocytic system, from internalization to mRNA escape, to infer the correlation between amount of LNP-mRNA in a compartment and escape. Out of 9 compartments tested, only EEA1, APPL1 and Rab11 compartments had positive differential correlations (Fig. 2a-b, **see Methods**). This suggests that, in the path from uptake to escape, mRNA sequentially traverses APPL1-, EEA1- and Rab11-positive compartments, with Rab11 endosomes having the highest probability for mRNA escape (Fig. 2b**, see Methods** and Extended Data Fig. 3a). This sequence is consistent with previous measurements of cargo flux through the endosomal system[16, 17]. LBPA- (multi-vesicular bodies, late endosomes), LAMP1- (late endosomes and lysosomes) and LC3-positive (autophagosomes) compartments have a negative or zero differential correlation (Fig. 2a), and, thus, are less likely to promote endosomal escape.

It is known that Rab5- and EEA1-positive endosomes gradually increase in size as they accumulate degradative cargo until they convert into late endosomes[18]. The small sized early endosomes actively sort recycling cargo through Rab11 endosomes whereas the large ones assume characteristics of multi-vesicular bodies (MVB) enriched in LBPA[19]. Given the low correlation of LBPA to delivery (Fig. 2a), we hypothesized that the small EEA1 endosomes are more competent to delivery than the large ones. Therefore, we analysed EEA1 endosomes with respect to mRNA delivery dependent on size, small (diameter <0.75 µm) and large (diameter >1.0 µm). We found that with time the large sized fraction increased (denoted as $EAA1_{large}$ in Fig. 2b) at the expense of the small sized ones in L608, MC3, and ACU5 LNP (Fig. 2c). Note that accumulation of LNP-mRNA in large-sized endosomes is not due to saturation of the endosomal system as only less than 5% of EEA1 endosomes contained LNP-mRNA during the initial two hours of uptake (Extended Data Fig. 4a). The finding that few (<5%), large early endosomes accumulate the majority (~90% at 2h) of LNP-mRNA suggests that their conversion into late endosomes is inhibited and they contribute minimally or not at all to delivery.

LNP differentially impair endosomal acidification leading to mRNA accumulation in non-productive compartments

A possible mechanism blocking early endosome maturation is suppression of endosomal acidification[20-22]. Therefore, to measure the pH of endosomes, we used ratiometric intensity measurements[23] of LDL conjugated to pH-sensitive Rodo-Red and pH-stable Alexa Fluor-488 probes co-internalised with LNP-Cy5-mRNA for 45, 120, and 180 min and imaged in living cells

(**see Methods**). The excessive amount of auto-fluorescence precluded the possibility to make such measurements in adipocytes. Therefore, we turned to HeLa cells as a well-established cell system and measured the effect of LNP on endosomal luminal pH. We first verified that HeLa cells could be transfected with LNP-mRNA (Supplementary Figure 5). In control cells that co-internalized the LDL probes without LNP-mRNA, 5% of LDL-positive structures had a pH of 6.5 and 74% a pH of 5.5, characteristic of early and late endosomes, respectively[24] (Fig. 3a, Supplementary Table 2). In contrast, a major fraction of LNP-Cy5-mRNA (L608-MOD5) containing endosomes had higher pH values (between early and late endosomes), i.e. failed to acidify to late endosomal pH, corroborating the hypothesis of endosomal maturation arrest. The percentage of arrested endosomes continued to increase over time (Supplementary Table 3). Interestingly, LNP formulations differed profoundly in their effects on endosomal acidification (Fig. 3a). The poorly endocytosed L319 LNP-Cy5-mRNA did not significantly affect endosomal acidification.

If endosomes are impaired in acidification, they may also fail to recycle LDL receptor to plasma membrane and thus reduce new LDL uptake. Consistent with this hypothesis, we found that the cells incubated with LNP-Cy5-mRNA that impairs endosomal acidification also show poor LDL uptake compare to the control and L319 LNP-Cy5-mRNA incubated cells (Extended Data Fig.6-7).

If endosomes are impaired in maturation (Fig. 2c, Extended Data Fig. 4a), acidification and cargo uptake, they are probably also unproductive for mRNA escape. A simple model of LNP propagation through endocytic compartments provided support to this idea (Extended Data Fig. 8a, **see Methods**). In this model, we considered two groups of endosomes, “active” (L_{act}) and “arrested” endosomes (L_{arr}). The eGFP degradation rate was taken from[25] and other parameters were deduced by fitting model predictions (Fig. 3b, lines) to experimentally measured ACU5 LNP-Cy5-mRNA intensity values in endosomes (Fig. 3b, black dots) and intensity of expressed eGFP (Fig. 3c, black dots) (**see Methods**). The best fit to experimental data predicted that escape from the arrested endosomes is negligible (Extended Data Fig. 8b; $esc_S = 10^{-5}$, 95% confidence interval $8.3\cdot10^{-6}\div1.2\cdot10^{-5}$), indeed suggesting that they do not contribute significantly to mRNA delivery.

Multi-colour single-molecule localization microscopy resolves singular LNP in endosomes with nanometer resolution

Our data point towards Rab11-, APPL1- and (non-arrested) EEA1-positive endosomes as potential sites for mRNA escape into the cytoplasm. All these compartments share tubular structures transporting recycling cargo, such as Transferrin, to the plasma membrane[16, 26-28]. We wondered whether recycling tubules may be preferential sites of mRNA escape into the cytosol.

Conventional light microscopy does not provide sufficient resolution to visualize mRNAs within endosomes or escaped. Therefore, we deployed multi-colour single-molecule localization microscopy (SMLM)[27]. The number of mRNA molecules per LNP range between 5 and 25 [13, 29] and each mRNA contains multiple Cy5 (average ~25 per mRNA, Trilink, L-7701), permitting to resolve the geometry of single LNP and even single Cy5-mRNA, i.e. stretched (max. length of 996 nucleotides ≈ 300 nm Trilink, L-7701) vs. condensed. We first benchmarked our SMLM approach by visualizing isolated LNP rested on glass surface at the nanoscale (**see Methods**). Extended Data Fig. 9 shows that individual LNP were visualized as isolated clusters of single molecule spots with median diameter ~60 nm. Smaller elongated clusters (ca. 25nm diameter) may correspond to damaged LNP or even dissociated Cy5-mRNAs (Extended Data Fig. 9).

Next, we performed triple-colour SMLM on cells having endocytosed both LNP and fluorescently-labelled cargo, Transferrin (Alexa Fluor 568) and EGF (Alexa Fluor 488) to label early-recycling and early-late endosomes, respectively[27]. In adipocytes, the large lipid droplets function as micro-lenses which distort the single molecule emission patterns. Therefore, we first performed SMLM in HeLa cells on the entire cell and then validated the observations in human primary adipocytes, by focusing on the endosomes underneath the plasma membrane by full TIRF. As we aimed at resolving mRNA localization within endosomes vs. cytosol, we refrained from using immunofluorescence labelling, which requires membrane permeabilization and may cause membrane leakage artefacts. We compared four LNP formulations with high, middle and low (L608, MC3, ACU5 and MOD5) eGFP expression. Strikingly, we could resolve individual LNP within endosomes labelled by EGF and/or Transferrin both in HeLa cells and primary human adipocytes (Fig. 4). Interestingly, singular LNP were most often associated with Transferrin-positive structures, i.e. within early-recycling compartments. To our knowledge, this is the first time that LNP are resolved by SMLM in sub-endosomal compartments. Based on our previous correlative ultrastructural analysis of early endosomes[27] clusters of single-molecule signals from labelled cargo in close proximity correspond to a single endosome (**see Methods**). Therefore, we quantified the size distribution of single LNP within endosomes by determining their full width at half maximal (FWHM) intensity (**see Methods**) and the calculated diameters (Fig. 4) are in good agreement with measurements of LNP size by dynamic light scattering (Supplementary Table 1) and SMLM on glass surface (Extended Data Fig. 9). Therefore, SMLM allows resolving individual LNP within sub-endosomal precision.

LNP accumulate in arrested endosomes, often lacking internalized EGF and Transferrin

For L608 and MC3 we consistently found a significant number of larger structures with an abundance of Cy5-mRNA signal in HeLa cells and primary human adipocytes (Fig. 5, Extended Data Fig. 10-19). Within these structures, in some cases individual LNP could be resolved (arrows in Fig. 5). We also detected large Cy5-mRNA-positive structures which either

correspond to LNP too closely located to be resolved (* in Fig. 5) or to dispersed Cy5-mRNA (** in Fig. 5). This suggests that some LNP are disassembled and the mRNAs released into the lumen of the endosomes. Interestingly, most of these large mRNA filled endosomes exhibited little EGF/Transferrin signal, in contrast to endosomes having no LNP, or small endosomes with a single LNP which contained internalized EGF/Transferrin (Fig. 5, Extended Data Fig. 10-19). These observations corroborate the pH measurement data of Fig. 3a showing that a significant fraction of endosomal structures with accumulated LNP are in an arrested state and, insulated from normal cargo uptake (Extended Data Fig. 6-7).

Multi-colour SMLM reveals mRNA escape from Transferrin-containing endosomal tubules

In many cases, we found Cy5-mRNA distinctly localized to Transferrin-positive tubules for all four LNP formulations (Fig. 6, Extended Data Fig. 15, 17-26). In the majority of such cases, the Cy5-mRNA signal could be observed alongside or at the very tip of tubules (Fig. 6a). Interestingly, we could also detect Cy5-mRNA signal which was not as intense and condensed as the single LNP shown in Fig. 4, but formed a pattern ranging from clustered to dispersed single molecule flashes (Fig. 6b). Such a signal was adjacent to, or outside of, Transferrin-positive structures, suggesting that this may correspond to mRNA escaped or in the process of escaping (Fig. 6b). Strikingly, in very rare cases, we could resolve Cy5 flashes ordered along a smooth line spanning a tubule and projecting into the cytoplasm (Fig. 6c). We interpret these events as capturing the escape of the mRNA from the endosomal tubule. This interpretation is supported by several lines of evidence. First, most mRNA signal has the nanoscopic appearance of single LNP and is associated with endosomal structures easily recognizable by the presence of EGF/Transferrin. Cy5-mRNA which does not colocalize with, or is in close proximity of, endosomal markers is most likely escaped into the cytoplasm. Second, as a control for false-positive Cy5-mRNA, only single LNP were visible predominantly in endosomes at the cell periphery after 30 min uptake of both LNP and EGF/Transferrin (Extended Data Fig. 28), but neither endosomal dispersed nor cytoplasmic mRNA signal was detectable. The combination of the HiLo illumination and the restriction of the fitted FWHM results in a reasonably narrow axial distribution of mRNA localizations in our SMLM images (Extended Data Fig. 29). Therefore, a random axial colocalization of distinct Cy5-mRNA signal to Transferrin tubules can be excluded with great certainty. Third, the frequency of signal outside of endosomes was 6.9% ± 1.5 (L608), 5.9% ± 1.3 (MC3), 4.0% ± 0.7 (MOD5) and 3.0% ± 0.9 (ACU5) (mean ± SD), consistent with a very low probability of endosomal escape (**see Methods**). Fourth, the observed patterns did not change during the time of acquisition, ruling out sample drift or diffusion artefacts (Extended Data Fig. 30). Fifth, escape events could also be detected at endosomes containing multiple LNP and Transferrin, i.e. competent for cargo transport. The Cy5 signal resembling stretched mRNA molecules, was exclusively associated with the Transferrin tubules and nowhere else at the

object perimeter (Fig. 6d). Sixth, we consistently found similar events in primary human adipocytes and HeLa cells (Fig. 6, Extended Data Fig. 15, 17-26), substantiating the notion that mRNA escape from Transferrin-positive tubules is a general mechanism contributing to effective transfection and shared by different cell types.

Altogether, SMLM allows distinguishing intracellular Cy5-mRNA into three categories, condensed LNP, dispersed within endosomes and a small fraction of non-endosomal de-condensed signal which is consistent with escaped cytoplasmic mRNA.

Discussion

The biggest challenge in the development of mRNA, and macromolecular therapeutics in general (siRNA, CRISPR/Cas9, antibodies, etc.), is delivery to both specific target cells and correct intracellular site of function (cytoplasm or nucleus). Crossing the endosomal membrane remains a major challenge, currently restricted to a small fraction of exogenous macromolecules, thus limiting their potential as therapeutics. In this study, we aimed to identify endosomal compartments which are most favourable to mRNA escape. To identify key parameters predicting efficient LNP-mRNA delivery, we performed a comparative image-based analysis on intracellular trafficking of six LNP with distinct chemical composition and efficiency in primary human adipocytes. Contrary to what is generally assumed[10, 30], our analysis revealed that delivery efficacy is not proportional to total cellular uptake. For some LNP-mRNA formulations, a large fraction accumulates in a small population of early endosomes that progressively become defective in acidification, cargo transport and, importantly, delivery (Fig. 7). We further discovered that endosomal recycling compartments have the highest probability of mRNA escape. Strikingly, by single molecule microscopy techniques we could resolve individual LNP within endosomes and capture rare events of single mRNA molecules in the process of escaping from Transferrin-containing tubules. Our results define quantitative endosomal parameters that can guide the development of new mRNA formulations towards high efficacy and low cytotoxicity.

Most LNP follow the standard endocytic route of degradative cargo, i.e. accumulate in few large early endosomes before progression to late endosomes/lysosomes. SMLM resolved the presence of single LNP but also of large unstructured aggregates within large early (Transferrin-positive) endosomes. An important finding was that such LNP accumulation is accompanied by endosome acidification defects. One potential reason could be protonation of ionisable cationic lipids in the formulation that may produce buffering effects similar to the proton sponge mechanism[10]. Such defect cannot persist over time if the V-ATPase maintaining the pH of endosomes remains functional. However, ionisable LNP lipids may also interfere with

ATPase proton pumps[31]. Alternatively, ionisable lipids may increase the leakiness of endosomal membrane to protons. Because acidification is critical to various endosomal activities, such as protein sorting, endosomal progression, lysosomal degradation and cellular homeostasis in general, LNP accumulation has a series of cytotoxic consequences. As endo-lysosomal hydrolytic enzymes require acidic pH[32], suppressed acidification will prevent the biodegradation of the LNP lipids even if *per se* bio-degradable, thus exacerbating LNP accumulation. LNP uptake is typically mediated by LDL receptor (LDLR)[33], and since LDL-LDLR dissociation requires acidic pH, without acidification LDLR will not recycle to the surface[34], thus blocking further uptake. This is consistent with the lower rates of LNP uptake and later times of internalization (Fig. 1b). The endosomal maturation arrest and accumulation of undegraded LNP is reminiscent of lysosomal storage disorders[35, 36]. In addition to cytotoxicity, these alterations may cause an inflammatory response, similar to the immune system defects characterizing lysosomal storage disorders[37]. Therefore, defective endosomal acidification may account for a great deal of the cytotoxic effects of LNP[38, 39]. SMLM revealed several types of arrested endosomes consistently in adipocytes and HeLa cells, suggesting that this may be a common defect. Interestingly, despite the abundance of LNP-mRNA in enlarged endosomes, we never detected mRNA escape events associated with them. We interpret these endosomes as incompetent for mRNA delivery, in agreement with the correlation analysis.

Previous reports on siRNA delivery have concluded that escape occurs mainly from Rab5- and Rab7- but not EEA1- and LAMP1-positive endosomes[40]. Our analysis partially confirmed these conclusions for mRNA but further revealed that APPL1, a sub-population of EEA1-, and Rab11-positive recycling endosomes have the highest probability of delivery by the LNP tested. These compartments share a high proportion of tubular recycling structures[16, 28]. Consistent with this interpretation, SMLM visualized endosomal mRNA escape events from Transferrin-positive recycling tubules both in primary human adipocytes and HeLa cells at the nanoscale. These results corroborate our conclusion that LNP-mediated cargo escape occurs in a limited time window during transport along the endocytic pathway[15].

What makes endocytic/recycling endosomes particularly favourable to macromolecule escape? Multiple potential mechanisms have been proposed, such as proton sponge and subsequent endosomal bursting, cationic lipid based membrane destabilization and pore formation-mediated membrane fusion[10]. However, none of these mechanisms have received compelling experimental support and endosome bursting appears restricted to lipoplexes but not applicable to LNP[15, 40]. The accumulation of undeliverable LNP-mRNA in endosomes does not support the hypothesis of endosome disruption by the proton sponge mechanism and argues that retarding cargo degradation along the endosomal pathway may not increase the chance for cargo escape but rather contribute to toxic effects. It is possible that multiple mechanisms are in play depending on differences in LNP composition and surface properties,

macromolecules and their transport. Our data argue for a new mechanism. Endosomal recycling tubules are characterized by high positive curvature along the tubules and sharp transition to negative curvature at the neck of the tubules. Exogenous cationic lipids may interfere with the packing of lipids in the membrane bilayer, resulting in local instability and, thus, membrane leakage. In addition, recycling tubule fission could create spontaneous breakage of the membrane that may favour macromolecular escape. Therefore, we propose that endosomes with recycling tubular structures are hotspots for mRNA escape events (Fig. 7).

Our results provide guidance for new delivery systems design strategies aimed to target recycling endosomes to improve macromolecule escape. A possible strategy would be to develop LNP that can be distributed more evenly between endosomes or even preferentially sorted to recycling tubules. For this, extended binding to LDLR may prolong the resident time in recycling endosomes, increase efficacy and decrease toxicity.

Methods

Cell culture:

Human adipose stem cells (hASCs) were obtained from patients undergoing elective surgery at Sahlgrenska University Hospital in Gothenburg, Sweden, all of which received written and oral information before giving written informed consent for the use of the tissue. The studies were approved by The Regional Ethical Review Board in Gothenburg, Sweden. All procedures performed in studies involving human participants were in accordance with the ethical standards of the institutional and national research committee and with the 1964 Helsinki declaration and its later amendments or comparable ethical standards. All subjects complied with ethical regulations. hASCs were tested negative for mycoplasma. We adapted previously published protocol [41] from AstraZeneca (AZ) to differentiate hASCs to mature white-like adipocytes in 384 well format. Briefly, EGM-2 proliferation medium was prepared according to the manufacture's protocol with EBM-2 medium supplemented with 5% FBS, all provided supplements, except hydrocortisone and GA-1000 (Lonza, Cat No. 3202, EGMTM-2 MV BulletKitTM (CC-3156 & CC-41472). Cryopreserved human adipose stem cells were then resuspended in EGM-2 medium and centrifuged at 200xg for 5min. Cells were counted with a CASY cell counter (Schärfe System) and 4000 cells per well were seeded in 50 µl EGM-2 medium containing 50 U/ml penicillin and 50µg/ml streptomycin (P/S) (Gibco, 15140-122) into 384 well plates (Greiner Bio-One, 781092) using the drop dispenser Multidrop. The cells were cultured at 37˚C and 5% CO_2 for 3 to 4 days. For adipocyte differentiation, 90% confluent cells were incubated for 1 week with Basal Medium (Zenbio, BM-1) supplemented with 3% FBS Superior, 1µM dexamethasone (Sigma Aldrich), 500µM 3-isobutyl-1-methyxanthine (Sigma Aldrich), 1µM pioglitazone (provided by AZ), P/S and 100 nM insulin (Actrapid Novonordisk, provided by AZ). Medium was replaced with BM-1 medium supplemented with 3% FBS Superior, 1µM dexamethasone, P/S and 100nM insulin and cells were incubated for another 5 days.

HeLa cells were cultured in DMEM media supplemented with 10% FBS Superior (Merck, S0615) and 50µg/mL Gentamycin (Gibco, G1397) at 37°C with 5% CO_2. For LNP trafection for eGFP expression and endosomal pH measurement studies, 3000 HeLa cells/well were seeded in

384 well plates using the drop dispenser (Multidrop, Thermo Fischer Scientific) one day prior to experiment.

Chemicals and reagents:

FBS Superior (Merck, S0615), dexamethasone (Sigma Aldrich, D2915), 3-isobutyl-1-methyxanthine (Sigma Aldrich, I5879). Insulin (Actrapid Novonordisk) and Pioglitazone (AZ10080838) are provided by Astra Zeneca. Penicillin and Streptomycin (Gibco, 15140-122), Transferrin Alexa-568 (Invitrogen™, T23365), EGF Alexa-488 (Invitrogen™, E13345), LDL-pHRodo (Invitrogen ™, L34356), LDL-Alexa 488 was homemade, as previously reported [27]. pH calibration buffers (Invitrogen™, P35379). LNP were prepared using the cationic ionizable lipids, ((2-(dimethylamino)ethyl)azanediyl)bis(hexane-6,1-diyl)bis(2-hexyldecanoate) (MC3), L608, ACU5, ACU22, MOD5 and L319 (AstraZeneca), and the helper lipids cholesterol (Sigma Aldrich), 1,2-distearoyl-sn-glycero-3-phosphocholine (DSPC, CordenPharma), 1,2-dimyristoyl-sn-glycero-3-phosphoethanolamine-N [methoxy (polyethyleneglycol)-2000] (DMPE-PEG2000, NOF Corporation) and contained CleanCap® Enhanced Green Fluorescent Protein (eGFP) mRNA (5-methoxyuridine)and/or Clean Cap®Cyanine5 (Cy5) Enhanced Green Fluorescent Protein mRNA (5-methoxyuridine) (TriLink Biotechnologies). Formaldehyde (Merck), Digitonin (Sigma Aldrich).

LNP mRNA formulation and characterization:

All LNP were formulated by a bottom-up approach[42] using a NanoAssemblr microfluidic apparatus (Precision NanoSystems Inc.). Lipids were characterized by NMR for quality control (Extended Data Fig. 31). Prior to mixing, the lipids were dissolved in ethanol and mixed in the appropriate molar ratios (cationic ionizable lipid:DSPC:cholesterol:DMPE-PEG ratios of 50:10:38.5:1.5) while mRNA was diluted in RNase free 50 mM citrate buffer pH 3.0 (Teknova). The aqueous and ethanol solutions were mixed in a 3:1 volume ratio at a mixing rate of 12 mL/min to obtain LNP with a mRNA:lipid weight ratio of 10:1. Finally, they were dialyzed overnight using Slide-A-Lyzer G2 dialysis cassettes with a molecular weight cutoff of 10 K

(Thermo Scientific). The size was determined by DLS measurements using a Zetasizer Nano ZS (Malvern Instruments Ltd.) The encapsulation and concentration of mRNA were determined using the Ribo-Green assay (Supplementary Table 1).

LNP mRNA uptake:

For both mature human white-like adipocytes and HeLa cell experiments, LNP at a final mRNA concentration of 1.25ng/µl was incubated at indicated time points in the figures. Mature human white-like adipocytes were transfected in the presence of fresh BM-1 medium supplemented with 1% human serum (Sigma, H4522) to mimic the subcutaneous tissue environment. HeLa cells were transfected in the presence of 10% FBS Superior. LNP addition on 384well plates was done either using automated liquid handling robot Fluent or manual multichannel pipettes.

Combined immuno-fluorescence and single molecule fluorescence in situ hybridization staining:

Endosomes and unlabelled mRNA formulated LNP were labelled by immuno-fluorescence (IFS) and smFISH, respectively. We used an optimized protocol compatible with quantitative retention of the delivered mRNA in the cell cytoplasm [manuscript under review]. Briefly, cells incubated with LNP-mRNA were washed with PBS, fixed with freshly prepared 7.4% formaldehyde for 2h, washed 3 times with PBS and permeabilized with 0.004% Digitonin for 2min (Note: Digitonin was first purified using manufacturer's protocol (product number D5628). Due to batch variations of this natural product, we recommend to optimize the concentration for each new purchase). After permeabilization, cells were washed and incubated with 3% BSA-PBS blocking solution for 30 to 45min. Primary antibodies prepared in 3% BSA-PBS solution were incubated for 2h and then washed 3 times with PBS. Secondary antibodies (final concentration of 3% BSA PBS solution) were incubated for 1h and washed 3 times with PBS. After this step, cells were fixed second time with 3.7% FA for 10min to preserve antibody staining and before proceeding for smFISH to fluorescently label mRNAs. The cells were washed

3 times with PBS, the supernatant was removed manually with an 8-needle aspirator and 70% Ethanol was added for 1h. After washing the cells with PBS using the Power Washer 384 (PW384, Tecan), Wash Buffer A (40 µl/well) was added for 2-5min. The supernatant was removed and eGFP - CAL Fluor® Red 590 Dye probe, from Stellaris® was diluted 1:100 in Hybridization Buffer (12.5µl/well) and incubated with cells for 16h at 37°C. The supernatant was removed, washed 2 times by incubating 40µL Wash Buffer A for 30min at 37°C. Cells were then washed again with Wash Buffer B for 2-5min. Finally, cells were incubated with DAPI (1µg/mL) to stain the nuclei and or CMB (0.25µg/mL) to stain the cytoplasm. All solutions were prepared in nuclease free PBS and all blocking and antibody solutions were mixed with 1X final concentration of nuclease inhibitors. Most washing steps and addition of solutions were performed via automated liquid handling robotic systems. All antibodies used in this study and their dilutions are given in Supplementary Table 4. We avoided double antibody staining in order to keep the green fluorescent channel free to subtract auto-fluorescence from adipocytes by image analysis methods.

Fluorescence imaging and quantification:

All confocal imaging was performed on an automated spinning disc confocal microscope (Yokogawa CV7000) using a 60x 1.2NA objective. In all cases, at least 6 images were acquired per well and each condition was in triplicate wells.

Image analysis was performed using a custom-designed software, MotionTracking [43] (http://motiontracking.mpi-cbg.de). Images were first corrected for illumination, chromatic aberration and physical shift using multicolour beads. All fluorescent objects in corrected images were then segmented, their number and intensity per image mask area were calculated. Cells differentiated into fibroblasts in the same culture were excluded by mask image generated by lipid droplets of adipocytes using a Fiji script. For kinetics and co-localization correlation analysis, the auto-fluorescence objects were eliminated using green channel as a base. First, the images taken by exciting green laser was used to segment auto-fluorescence objects. mRNA objects (CAL Fluor® Red 590 Dye) co-localizing to auto-fluorescence objects were then excluded

from the analysis. The quality of the quantification was verified by internal non treated control cells.

Co-localization and statistical analysis were performed using the MotionTracking software. Co-localization of mRNA to endosomal compartments was performed with a threshold of 35% and corrected for random co-localization as described previously [44]. Image analysis was also done using Fiji [45] and CellProfiler [46] software. Briefly, corrected images were pre-processed for segmentation in Fiji, LNP spots and nuclei were segmented and quantified in CellProfiler. Some data from MotionTracking were loaded in KNIME [47] for visualization with customized R scripts.

Differential correlation analysis:

For correlation analysis of mRNA distribution in endosomal compartments and eGFP expression, we chose a specific time point in LNP kinetics based on two criteria to exclude false predictions: 1) LNP mRNA signal in the endosomal compartments is above the noise level. We used LNP L319 (both uptake and eGFP expression) as an internal control due to its low uptake. 2) A time point prior to mRNA saturation in endosomal compartments.

The LNP-mRNA traffic through endocytic compartments could be drawn as a directed acyclic graph (DAG), where the nodes of the graph denote the compartments and directed edges (arrows) denote the direction of cargo flow. We expanded such presentation by adding a master node A (Extended Data Fig. 3a) to denote total uptake of LNP-mRNA by the endocytic system and node Ex to denote release of mRNA to cytoplasm (specifically, expression of eGFP as a proxy for mRNA release). The edges of such an extended graph represent cause-consequence dependencies between amounts of cargo in the endocytic compartments. Indeed, total uptake A is the cause of the amount of LNP-mRNA in compartment C, and the amount of LNP-mRNA in D depends on C, etc. The correlation between the amount of LNP-mRNA in any endocytic compartment and the amount of released mRNA (Ex) decreases proportionally to the stochasticity of the edges connecting these two nodes (regardless of the direction of connections). Indeed, total mRNA escape (node Ex) correlates with all compartments which

receive LNP-mRNA from node A (nodes B-F). However, since the escape occurs from compartment D, the correlation between amount of LNP-mRNA in D and eGFP expression is the largest (r_6). The correlation of the upstream compartment C to eGFP expression Ex is equal to $r_{C\text{->}Ex} = r_3 * r_6$, where r_3 is correlation between the amounts of LNP-mRNA in compartment C and D, and thus lower than r_6. Therefore, we chose $r_{A\text{->}Ex}$ of total LNP-mRNA uptake (A) to eGFP expression (Ex) as a baseline and subtracted it from the correlations of amount LNP-mRNA in each endocytic compartment to eGFP expression in order to get the differential correlation. It is obvious, that compartments on the path from uptake A to escape Ex (but not only them) have a differential correlation above zero. On the other hand, compartments with differential correlations below zero are located on side branches of the graph (e.g. E, F, and B). Therefore, by ranking compartments according to the differential correlation, such analysis allows reconstructing the DAG of causal dependencies for mRNA delivery (see Fig 2a & b).

Uncertainty estimation for correlation:

Let's assume that we have two zero-mean experimental vectors $\{a_i\}$ and $\{b_i\}$ with per-element uncertainty estimation $\{\delta a_i\}$ and $\{\delta b_i\}$. If elements a_i and b_i are means of experimental measurements, then δa_i and δb_i are SEMs.

The correlation is $r = \dfrac{\sum_{i=1}^{N} a_i b_i}{\sum_{i=1}^{N} a_i^2 \sum_{i=1}^{N} b_i^2}$

Let us assume that uncertainties of vector elements are independent and drawn from normal distribution. For example, if the elements are mean of experimental measurements, then this assumption is correct as a result of central limit theorem.

Given such assumption, the variance of correlation can be estimated as:

$$D(r)=\frac{\sum_{j=1}^{N}\left(\frac{\partial r}{\partial a_j}\delta a_j\right)^2+\sum_{j=1}^{N}\left(\frac{\partial r}{\partial b_j}\delta b_j\right)^2}{N}$$

After substitution the final expression for variance of correlation is:

$$D(r)=\frac{\sum_{j=1}^{N}\left(\left(b_j-a_jc_a\right)\delta a_j\right)^2+\sum_{j=1}^{N}\left(\left(a_j-b_jc_b\right)\delta b_j\right)^2}{N\sum_{i=1}^{N}a_i^2\sum_{i=1}^{N}b_i^2}$$

where

$$c_a=\frac{\sum_{i=1}^{N}a_ib_i}{\sum_{i=1}^{N}a_i^2} \text{ and } c_b=\frac{\sum_{i=1}^{N}a_ib_i}{\sum_{i=1}^{N}b_i^2}$$

One can see, that if $r\to 1$ and $a_i\cdot b_i>0$, then $D(r)\to 0$ independent on uncertainty δa_i and δb_i.

DAG graphical schemes were prepared in Adobe Photoshop 2020 and Inkscape software.

Ratiometric pH measurement by LDL probes:

HeLa cells were seeded one day prior to transfection either in 96 or 384 well plates at a density of 12,000cells/well or 3000cells/well, respectively. pH measurements of LNP-mRNA-positive endosomes were determined by ratiometric analysis of intensities of pH sensitive LDL pHRodo-Red and pH stable LDL- Alexa 488 probes, similar to previously reported [23]. Briefly, LNP-mRNA (1.25ng/µl) with or without LDL pHRodo-Red (20µg/mL) and LDL Alexa-488 (1:100 from homemade stock, **see Chemicals and reagents**) were co-internalized in cells for 45min, 2h, 3h imaged live and fixed at the end of the experiment. The pH calibration measurements were

performed on each plate. LDL-pHRodo-Red/LDL-Alexa-488 were co-internalized in HeLa cells for 3h. Cells were fixed (3.7% FA, 10min), and incubated with pH = 4.5, 5.5, 6.5 and 7.5 calibration buffers (ThermoFisher, P35379) with DAPI/CMB and equilibrated for at least 2h. cells were imaged using an automated spinning disc confocal microscope (Yokogawa CV7000) 60X, 1.2NA (Extended Data Fig. 32). The intensity of pHRodo-Red increased ~30 fold when pH decreased from 7.5 to 4.5.

Images were segmented using the MotionTracking software and individual endosomes identified. Integral intensities were calculated for both LDL probes and the ratio of integral intensities was determined. The calibration of ratios of integral intensity was performed for each individual experiment (Extended Data Fig. 33). Surprisingly, the distributions of ratios significantly varied between experiments and were multimodal for all pH values. Such wide multimodal distribution does not allow to use the mean value of ratios of calibration measurements as a coefficient to convert ratios into pH for the live cell measurements (Extended Data Fig. 34)

We hypothesized that the ratio of distributions could be described as the sum of log-normal distribution and used Bayesian analysis to find how many components are required to describe them [48]. From this, we found that the most probable number of components was 3. Therefore, we globally (simultaneously) fit the calibration of distributions of 3 independent experiments by the sum of log-normal components, keeping the parameters of components equal for the experiments, but allowing different amplitudes:

$$y_j(x) = \sum_{i=1}^{3} \frac{A_{i,j}}{\sqrt{2\pi}\sigma_i x} e^{-\frac{1}{2\sigma_i^2}\ln\left(\frac{x}{\mu_i}\right)^2}$$

where $y_j(x)$ is the model distribution of ratios in the repeat *j*; x is ratio of intensities; μ_i, σ_i are parameters of component *i*, $A_{i,j}$ is the contribution of component *i* in the repeat *j*. The resulting parameters μ_i, σ_i as function of pH are presented on Extended Data Fig. 35. Given, that the fit was performed independently for each pH, the smooth changes of parameters values with pH circumstantially support our 3-component model.

The deduced parameters allowed us to interpolate intensities ratio distributions for intermediate values of pH (Extended Data Fig. 36).

In order to find the pH distribution in endocytic compartments, we divided the pH interval from 4.5 to 7.5 on bins by steps of 0.05 units. We introduced amplitudes of all 3 components for each bin ($A_i(pH)$, i = 1,2,3) and used them as free variables to fit theoretical distribution to experimental data (Extended Data Fig. 37a). The fit was performed by library Climb of MotionTracking software. Finally, the pH distribution was calculated as a sum of amplitudes of all 3 components in each pH bin: $y(pH) = \sum_{i=1}^{3} A_i(pH)$. The results of such fit for 3 independent experiments are presented on (Extended Data Fig. 37b).

Despite differences in calibration distributions of experimental repeats (Extended Data Fig. 33), the predicted pH distributions of independent experiments are very much in agreement with each other (Extended Data Fig. 37b) and, as such, provide additional support to our model.

LNP uptake and eGFP expression kinetics measurements:

For determining the arrested endosomes contribution to mRNA escape, we used ACU5 LNP formulated with either unlabelled (eGFP expression) or Cy5 fluorophore labelled mRNA (uptake). Adipocytes were incubated with ACU5 mRNA formulation for 20min, 30min, 45min, 60min, 2h, 4h, 6h, 8h, 12h, 24h and fixed with optimized protocol [manuscript under review]. The cells were then stained for nuclei (DAPI 1µg/ml) and cytoplasm (CMB 0.5µg/mL), imaged using an automated confocal microscope (Yokogawa CV7000), the total eGFP intensity and the segmented mRNA intensities were analysed using the MotionTracking software.

Model for prediction of mRNA escape from arrested endosomes:

Experimental data and theoretical model were combined to determine the contribution of the maturation arrested endosomes to mRNA escape. In our model, we considered two groups of endosomes – “active” and “arrested”. The LNP propagate through “active” early

endosomes and either route towards late endosomes and lysosomes for degradation or long-living "arrested" endosomes. The amount of LNP in "active" and "arrested" endosomes are respectively denoted as L_e and L_s (Extended Data Fig. 8a. eq. (1) and (2)). The lag in LNP uptake is modelled by the transition function F(t). The amount of LDL receptors (LDLR) on the plasma membrane is denoted by R (eq.(1) and (3)). Surprisingly, we found that we could explain the declining LNP uptake (between 8h-24h, Figure 3b, Black dots) without assuming that a massive uptake of LNP leads to the downregulation of LDLR from the plasma membrane (eq. (3)). This led us to hypothesize that the "arrested" endosomes are not sufficiently acidic to release LNP from LDLR, thus preventing its recycling to the plasma membrane. This process was modelled by eq. (3). The fraction of mRNA that leaks from early "active" and "arrested" endosomes are described by eq. (4), where esc_s denotes the ratio of mRNA leakage from "arrested" to "active" endosomes. The eq. (5) describes the synthesis and degradation of eGFP [25].

Single molecule localization microscopy:

Cover-glasses of 24mm diameter were first sonicated in 70% ethanol for 5min and washed 3 times using autoclaved water and PBS. The clean cover glasses were distributed on 6 well plate and seeded HeLa cells at a density of either 200,000 cells prior to one day of the experiment. Human primary adipose stem cells were seeded at the density of 500,000 cells and differentiated to adipocytes as mentioned in cell culture methods. The cells were incubated with LNP-mRNA (at a final mRNA concentration of 1.25ng/µl) for total of 120min. EGF-Alexa 488 (100ng/mL) and Transferrin-Alexa 568 (10µg/mL) or homemade LDL-Alexa 488 (1:100 dilutions, **see Chemicals and reagents**) was incubated for last 30min of LNP uptake. LNP incubation in HeLa cells were supplemented with 10% FBS and primary human adipocytes supplemented with 1% Human serum. The cells were then fixed with 7.4% FA for 2h, washed 3 times with PBS.

Multi-color SMLM experiments were performed on a Nikon Eclipse Ti microscope, which is specified elsewhere in detail[27]. Prior to acquisition, cells were irradiated in epifluorescence illumination mode to turn emitters, which were out-of-focus in the HILO illumination scheme, into the dark state. In all experiments, the length of the acquisition was set to capture the

majority of emitters, i.e. imaging was concluded when only a very minor number of active emitters was detectable. Typical acquisition lengths were 30000-60000 frames for 641 and 561 nm and 15000-30000 frames for 488 nm excitation, respectively. Hereby, mEOS2 was excited at 561 nm and activated with 405 nm. Raw image stacks were analysed with rapidSTORM 3.2 [49]. The FWHM was set as a free fit parameter, but in the limits of 275–475 nm for 561 nm and 640 nm and 275-450 nm for 488 nm excitation, respectively. This way, we allow only a narrow axial range (ca. 500 nm)[50] to contribute to the final SMLM data set, in order to minimize the likelihood of random axial colocalization. The fit window radius to 1200 nm, while all other fit parameters were kept from the default settings in rapidSTORM 3.2. Linear lateral drift correction was applied manually by spatio-temporally aligning distinct structures to themselves. This was facilitated by color-coding of the temporal coordinate with the built-in tool. Same tool was used to create spatio-temporal images of mRNA escape events (Extended Data Fig. X17).

Prior to imaging of samples, a glass surface with Tetraspeck beads (Thermo Scientific) was imaged with alternating 488 nm, 561 nm and 641 nm excitation to create a nanometer precise map to allow the correction of chromatic shift.

Candidates for single LNP were selected in the range of 25 – 250 nm on the basis of previously reported LNP diameters. FWHMs were determined from the super-resolved images (10 nm pixelsize) by Gaussian fitting. Mean diameters for LNP in cells were determined to 74.9nm ± 22.6 (mean ± SD) for L608, 71.0nm ± 22.0 for MC3, 66.7nm ± 20.2 for ACU5 and 68.9nm ± 21.7 for MOD5.

In adipocytes, large lipid droplets function as micro-lenses, making quantitative SMLM-based studies very challenging, since the three-dimensional distortions to the single molecule emission patterns negate the theoretical advantage of nm resolution. Therefore, we imaged only the endosomes underneath the plasma membrane at the bottom of adipocytes by full TIRF.

Estimation of cytosolic mRNA signal:

LNP/mRNA localizations were classified as non-cytosolic when satisfying one of the following criteria:

- Object is colocalized with endosomal cargo
- Object is localized within an arrested endosome
- Object is localized on cellular edge (cell border)

All other mRNA localizations not fulfilling at least one of the above criteria were considered likely to be cytosolic and the ratio regarding the total number of localizations was given.

However, it is important to consider that the photo-physical properties of the multiple Cy5 molecules per mRNA may vary between the different settings, i.e. mRNA cramped in a LNP, mRNA escaped or fully elongated in the cytosol. The actual fraction might therefore be even lower, since it is to be expected, that possible quenching effects between the dyes will occur predominantly in the densely packed environment of the intact LNP, thus reducing the localization count.

Acknowledgements:

We thank the following Services and Facilities of the Max Planck Institute of Molecular Cell Biology and Genetics for their support: Light Microscopy Facility (LMF) and the High-Throughput Technology Development Studio (HT-TDS) Facility. We thank the Center for Information Services and High Performance Computing (ZIH) of the TU Dresden for the generous provision of computing power. This work was financially supported by the Max Planck Society (MPG) and AstraZeneca.

Author contributions:

M.Z. and S.A. conceived the project, P.P., C.F., M.S. and M.B. designed the experiments. M.Y.A formulated and characterized LNP. P.P. and M.S. performed experiments in adipocytes and HeLa cells, analysed and interpreted the results. C.F. performed single molecule localization microscopy experiments, analysed data and interpreted the results. Y.K conceived the mathematical models for pH and endosomal escape from arrested endosomes, programmed and interpreted the results. M.Z., P.P., C.F., and Y.K. wrote the manuscript with edits by M.Y.A. M.S. M.B., A.H., S.B., A.S., L.L., A.D., A.B., and S.A. commented on results and interpretations. P.P. and C.F. contributed equally to this study.

Conflict of interest: A.H., S.B., A.S., L.L., M.Y.A., A.D., and S.A. are employed by AstraZeneca R&D Gothenburg, Sweden. A.B., is employed by AstraZeneca R&D, Boston, USA.

References

1. Coutinho, M.F., Matos, L., Santos, J.I. & Alves, S. RNA Therapeutics: How Far Have We Gone? *Advances in experimental medicine and biology* **1157**, 133-177 (2019).
2. Sahin, U. et al. COVID-19 vaccine BNT162b1 elicits human antibody and TH1 T cell responses. *Nature* **586**, 594-599 (2020).
3. Akinc, A. et al. The Onpattro story and the clinical translation of nanomedicines containing nucleic acid-based drugs. *Nature Nanotechnology* **14**, 1084-1087 (2019).
4. Dammes, N. & Peer, D. Paving the Road for RNA Therapeutics. *Trends in Pharmacological Sciences* **41**, 755-775 (2020).
5. Kose, N. et al. A lipid-encapsulated mRNA encoding a potently neutralizing human monoclonal antibody protects against chikungunya infection. *Science Immunology* **4**, eaaw6647 (2019).
6. Feldman, R.A. et al. mRNA vaccines against H10N8 and H7N9 influenza viruses of pandemic potential are immunogenic and well tolerated in healthy adults in phase 1 randomized clinical trials. *Vaccine* **37**, 3326-3334 (2019).
7. Kowalski, P.S., Rudra, A., Miao, L. & Anderson, D.G. Delivering the Messenger: Advances in Technologies for Therapeutic mRNA Delivery. *Molecular Therapy* **27**, 710-728 (2019).
8. Reichmuth, A.M., Oberli, M.A., Jaklenec, A., Langer, R. & Blankschtein, D. mRNA vaccine delivery using lipid nanoparticles. *Therapeutic Delivery* **7**, 319-334 (2016).
9. Wittrup, A. & Lieberman, J. Knocking down disease: a progress report on siRNA therapeutics. *Nat Rev Genet* **16**, 543-552 (2015).
10. Pei, D. & Buyanova, M. Overcoming Endosomal Entrapment in Drug Delivery. *Bioconjugate Chemistry* **30**, 273-283 (2019).
11. Sato, Y. et al. Highly specific delivery of siRNA to hepatocytes circumvents endothelial cell-mediated lipid nanoparticle-associated toxicity leading to the safe and efficacious decrease in the hepatitis B virus. *Journal of Controlled Release* **266**, 216-225 (2017).
12. Ahmad, J., Wahab, R., Siddiqui, M.A., Saquib, Q. & Al-Khedhairy, A.A. Cytotoxicity and cell death induced by engineered nanostructures (quantum dots and nanoparticles) in human cell lines. *JBIC Journal of Biological Inorganic Chemistry* **25**, 325-338 (2020).
13. Sabnis, S. et al. A Novel Amino Lipid Series for mRNA Delivery: Improved Endosomal Escape and Sustained Pharmacology and Safety in Non-human Primates. *Molecular Therapy* **26**, 1509-1519 (2018).
14. Maier, M.A. et al. Biodegradable Lipids Enabling Rapidly Eliminated Lipid Nanoparticles for Systemic Delivery of RNAi Therapeutics. *Molecular Therapy* **21**, 1570-1578 (2013).
15. Gilleron, J. et al. Image-based analysis of lipid nanoparticle-mediated siRNA delivery, intracellular trafficking and endosomal escape. *Nat Biotech* **31**, 638-646 (2013).
16. Kalaidzidis, I. et al. APPL endosomes are not obligatory endocytic intermediates but act as stable cargo-sorting compartments. *Journal of Cell Biology* **211**, 123-144 (2015).

17. Jovic, M., Sharma, M., Rahajeng, J. & Caplan, S. The early endosome: a busy sorting station for proteins at the crossroads. *Histology and histopathology* **25**, 99-112 (2010).

18. Rink, J., Ghigo, E., Kalaidzidis, Y. & Zerial, M. Rab Conversion as a Mechanism of Progression from Early to Late Endosomes. *Cell* **122**, 735-749 (2005).

19. Gruenberg, J. Life in the lumen: The multivesicular endosome. *Traffic (Copenhagen, Denmark)* **21**, 76-93 (2020).

20. Mauthe, M. et al. Chloroquine inhibits autophagic flux by decreasing autophagosome-lysosome fusion. *Autophagy* **14**, 1435-1455 (2018).

21. Yoshimori, T., Yamamoto, A., Moriyama, Y., Futai, M. & Tashiro, Y. Bafilomycin A1, a specific inhibitor of vacuolar-type H(+)-ATPase, inhibits acidification and protein degradation in lysosomes of cultured cells. *Journal of Biological Chemistry* **266**, 17707-17712 (1991).

22. Novikoff, A.B., Beaufay, H. & De Duve, C. Electron microscopy of lysosomerich fractions from rat liver. *J Biophys Biochem Cytol* **2**, 179-184 (1956).

23. Tycko, B. & Maxfield, F.R. Rapid acidification of endocytic vesicles containing alpha 2-macroglobulin. *Cell* **28**, 643-651 (1982).

24. Maxfield, F.R. & Yamashiro, D.J. in Immunobiology of Proteins and Peptides IV: T-Cell Recognition and Antigen Presentation. (ed. M.Z. Atassi) 189-198 (Springer US, Boston, MA; 1987).

25. Balleza, E., Kim, J.M. & Cluzel, P. Systematic characterization of maturation time of fluorescent proteins in living cells. *Nature Methods* **15**, 47-51 (2018).

26. Ullrich, O., Reinsch, S., Urbé, S., Zerial, M. & Parton, R.G. Rab11 regulates recycling through the pericentriolar recycling endosome. *The Journal of cell biology* **135**, 913-924 (1996).

27. Franke, C. et al. Correlative single-molecule localization microscopy and electron tomography reveals endosome nanoscale domains. *Traffic* **20**, 601-617 (2019).

28. Sönnichsen, B., De Renzis, S., Nielsen, E., Rietdorf, J. & Zerial, M. Distinct Membrane Domains on Endosomes in the Recycling Pathway Visualized by Multicolor Imaging of Rab4, Rab5, and Rab11. *Journal of Cell Biology* **149**, 901-914 (2000).

29. Yanez Arteta, M. et al. Successful reprogramming of cellular protein production through mRNA delivered by functionalized lipid nanoparticles. *Proceedings of the National Academy of Sciences* **115**, E3351-E3360 (2018).

30. Novakowski, S., Jiang, K., Prakash, G. & Kastrup, C. Delivery of mRNA to platelets using lipid nanoparticles. *Scientific Reports* **9**, 552 (2019).

31. Jones, P.C., Harrison, M.A., Kim, Y.I., Finbow, M.E. & Findlay, J.B. The first putative transmembrane helix of the 16 kDa proteolipid lines a pore in the Vo sector of the vacuolar H(+)-ATPase. *Biochem J* **312 (Pt 3)**, 739-747 (1995).

32. Dubland, J.A. & Francis, G.A. Lysosomal acid lipase: at the crossroads of normal and atherogenic cholesterol metabolism. *Front Cell Dev Biol* **3**, 3-3 (2015).

33. Akinc, A. et al. Targeted delivery of RNAi therapeutics with endogenous and exogenous ligand-based mechanisms. *Molecular therapy : the journal of the American Society of Gene Therapy* **18**, 1357-1364 (2010).

34. Bai, X. et al. Nanoparticles with High-Surface Negative-Charge Density Disturb the Metabolism of Low-Density Lipoprotein in Cells. *International journal of molecular sciences* **19** (2018).
35. Ballabio, A. & Gieselmann, V. Lysosomal disorders: From storage to cellular damage. *Biochimica et Biophysica Acta (BBA) - Molecular Cell Research* **1793**, 684-696 (2009).
36. Platt, F.M., Boland, B. & van der Spoel, A.C. Lysosomal storage disorders: The cellular impact of lysosomal dysfunction. *Journal of Cell Biology* **199**, 723-734 (2012).
37. Castaneda, J.A., Lim, M.J., Cooper, J.D. & Pearce, D.A. Immune system irregularities in lysosomal storage disorders. *Acta Neuropathologica* **115**, 159-174 (2008).
38. Garber, K. Worth the RISC? *Nature Biotechnology* **35**, 198-202 (2017).
39. Kulkarni, J.A., Cullis, P.R. & van der Meel, R. Lipid Nanoparticles Enabling Gene Therapies: From Concepts to Clinical Utility. *Nucleic Acid Therapeutics* **28**, 146-157 (2018).
40. Wittrup, A. et al. Visualizing lipid-formulated siRNA release from endosomes and target gene knockdown. *Nature Biotechnology* **33**, 870-876 (2015).
41. Bartesaghi, S. et al. Thermogenic Activity of UCP1 in Human White Fat-Derived Beige Adipocytes. *Molecular Endocrinology* **29**, 130-139 (2015).
42. Zhigaltsev, I.V. et al. Bottom-Up Design and Synthesis of Limit Size Lipid Nanoparticle Systems with Aqueous and Triglyceride Cores Using Millisecond Microfluidic Mixing. *Langmuir* **28**, 3633-3640 (2012).
43. Collinet, C. et al. Systems survey of endocytosis by multiparametric image analysis. *Nature* **464**, 243-249 (2010).
44. Kalaidzidis, Y., Kalaidzidis, I. & Zerial, M. A probabilistic method to quantify the colocalization of markers on intracellular vesicular structures visualized by light microscopy. *AIP Conference Proceedings* **1641**, 580-587 (2015).
45. Schindelin, J. et al. Fiji: an open-source platform for biological-image analysis. *Nature Methods* **9**, 676-682 (2012).
46. Carpenter, A.E. et al. CellProfiler: image analysis software for identifying and quantifying cell phenotypes. *Genome Biology* **7**, R100 (2006).
47. Berthold, M.R. et al. in Data Analysis, Machine Learning and Applications. (eds. C. Preisach, H. Burkhardt, L. Schmidt-Thieme & R. Decker) 319-326 (Springer Berlin Heidelberg, Berlin, Heidelberg; 2008).
48. Sivia, D.S. & Carlile, C.J. Molecular spectroscopy and Bayesian spectral analysis—how many lines are there? *The Journal of Chemical Physics* **96**, 170-178 (1992).
49. Wolter, S. et al. rapidSTORM: accurate, fast open-source software for localization microscopy. *Nat Methods* **9**, 1040-1041 (2012).
50. Franke, C., Sauer, M. & van de Linde, S. Photometry unlocks 3D information from 2D localization microscopy data. *Nature Methods* **14**, 41-44 (2017).

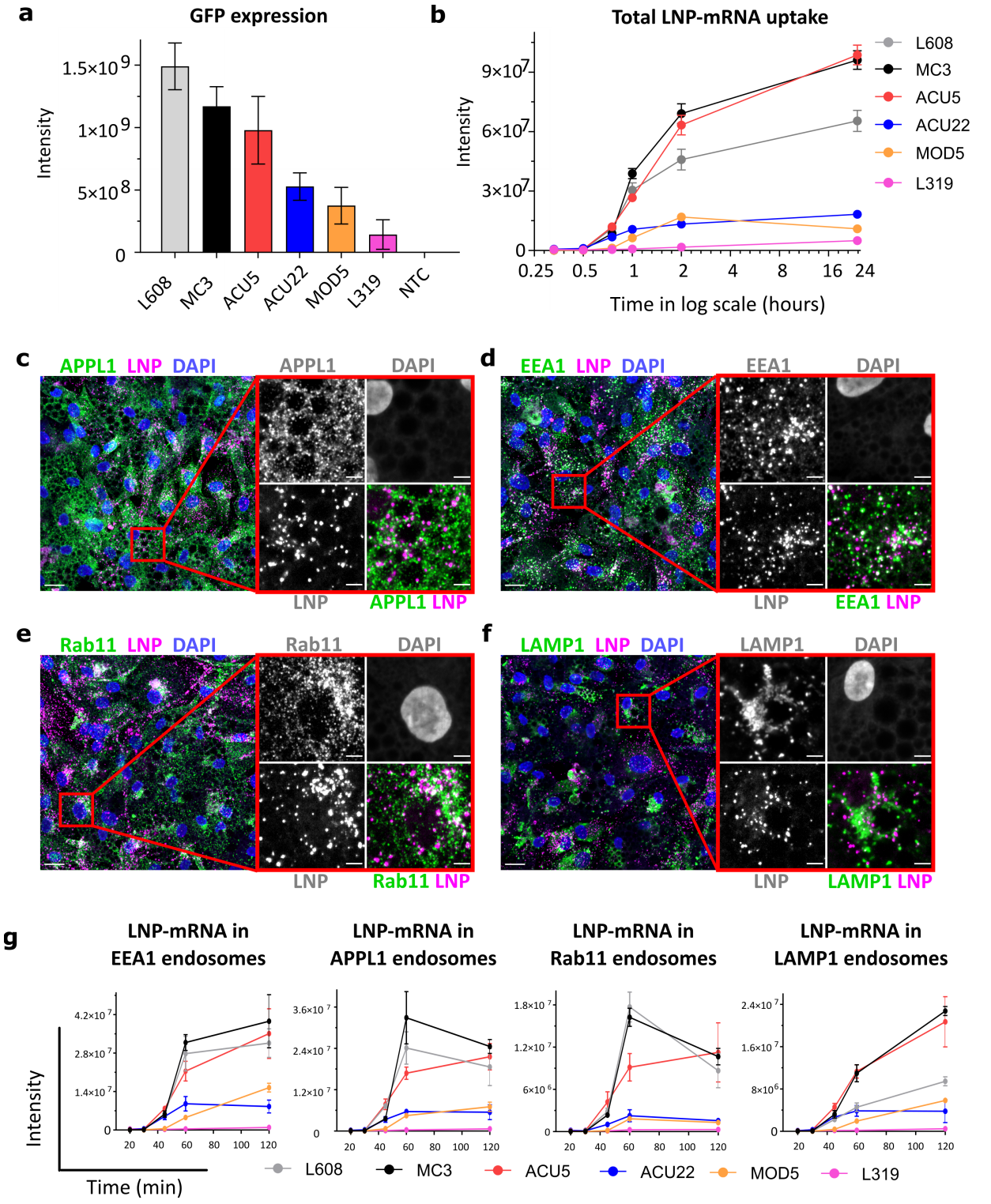

Figure 1: Comparative analysis of activity, endocytic uptake and endosomal distribution of six LNP-mRNA in primary human adipocytes. (**a**) Cells were incubated with various LNPs (1.25ng/µL) formulated with eGFP-mRNA, fixed, and imaged after 24h. The graph illustrates GFP expression for the indicated LNP-mRNA. N=3 independent experiments (mean ± s.e.m). (**b**) Cells incubated with LNP-mRNA as described above were fixed at the given time

point, processed for smFISH to fluorescently label mRNA and imaged by fluorescence microscopy. The quantification shows that LNP-mRNA uptake generally correlates to the GFP expression efficacy of LNP formulations displayed in panel **a** (Ex. MC3 Vs L319). (**c-f**) Representative images of human primary adipocytes incubated with L608 LNP-mRNA for 2h, immunostained with antibodies against endosomal markers (in green): APPL1 (c), EEA1 (d), Rab11 (e) and LAMP1 (f), exogenous mRNA detected by smFISH (labeled as LNP in the figure panel) and nuclei by DAPI. The magnified representative area is presented with split and merged color images. Bars indicate 20µm in the overview and 5µm in the magnified images. (**g**) Kinetics and endosomal distribution of the different LNP-mRNA incubated with cells as described in (c-f). N=3 replicates. (mean ± s.e.m).

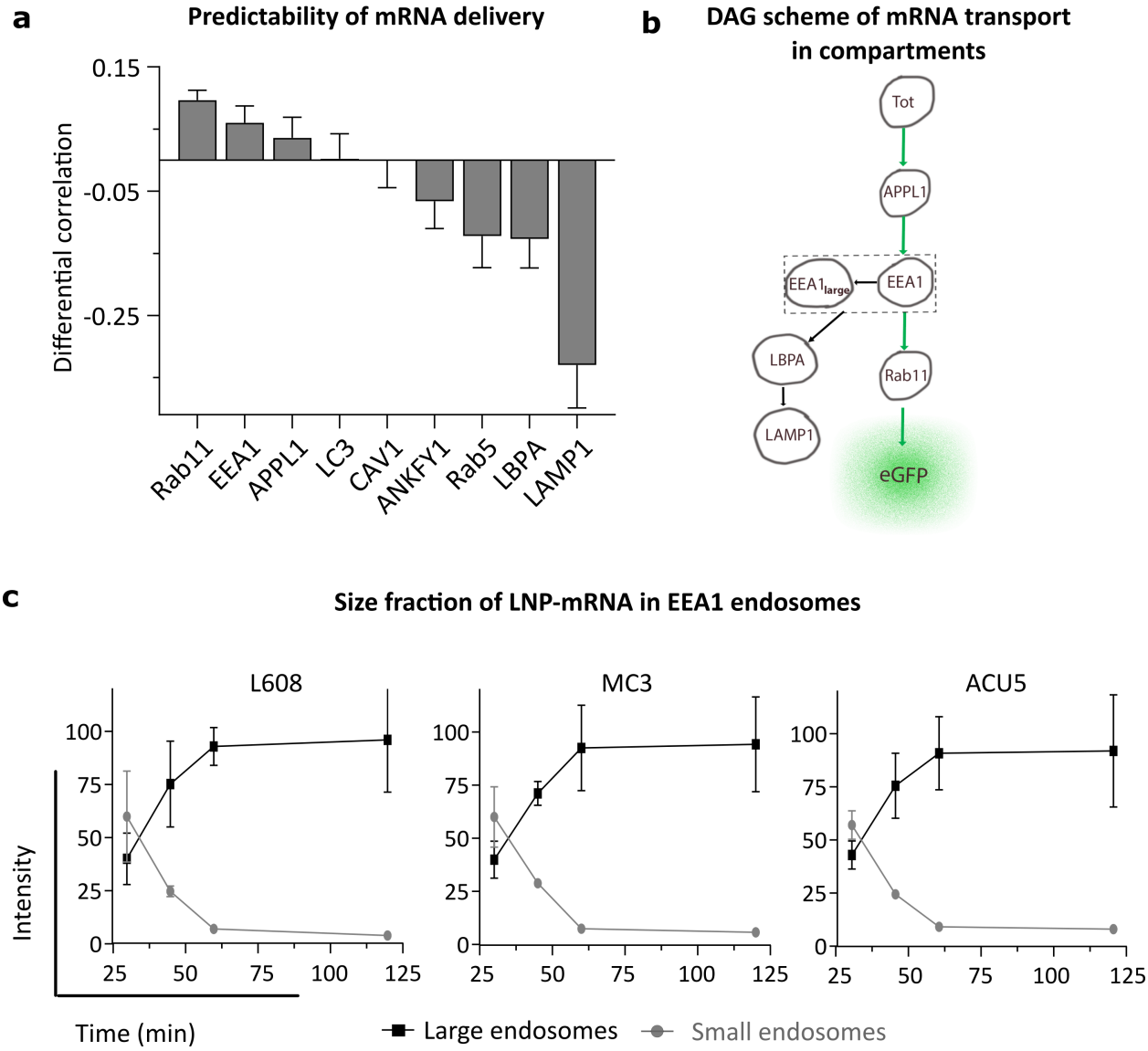

Figure 2: Differential correlation and size distribution kinetics analysis reveal that Rab11, small EEA1- and APPL1-positive endosomes are more favorable than other endosomal compartments for mRNA delivery. (a) The graph shows the differential correlation between LNP-mRNA distribution in 9 endosomal compartments to eGFP expression in human primary adipocytes (see **Methods**). Three compartments Rab11, EEA1 and APPL1 have correlation above total uptake and therefore are potential hotspots of mRNA escape, whereas e.g. Lamp1 is not. **(b) S**chematic representation of LNP-mRNA transport through endosomal compartments reconstructed based on the DAG differential correlation (panel **a**) and size fraction analysis (panel **c**). The total LNP-mRNA uptake is represented by node "Tot" which is upstream of the various endosomal compartments (represented by the indicated nodes) where cargo is sequentially distributed to. The Rab11 node is located close to the node eGFP because of its high correlation of LNP-mRNA distribution to eGFP expression (see **Methods**). Whereas the node EEA1 is upstream because it consists of small EEA1 LNP-mRNA endosomes that are productive for delivery, the large "arrested" ($EEA1_{large}$) endosomes are less/unproductive for LNP-mRNA delivery. **(c)** Quantification of LNP-

mRNA accumulation in EEA1 endosomes based on endosome size and intensity. The graph illustrates that the fraction of large LNP-mRNA endosomes (object diameter > 1µm) increases substantially whereas the smaller ones (object diameter = up to 0.75µm) decrease over time. Percentage decrease of small LNP-mRNA endosomes, L608 = 60.0% ± 14 to 5.7 ± 0.4; MC3 = 59.9% ± 21 to 4 ± 0.5; ACU5 = 57% ± 7 to 8% ± 1.0 Percentage increase of large LNP-mRNA endosomes, L608 = 40.0% ± 9 to 94.2 ± 22; MC3 = 40.0% ± 12 to 96.0 ± 24; ACU5 = 42.9% ± 7 to 92.3% ± 26. N=3 replicates, (mean ± s.e.m).

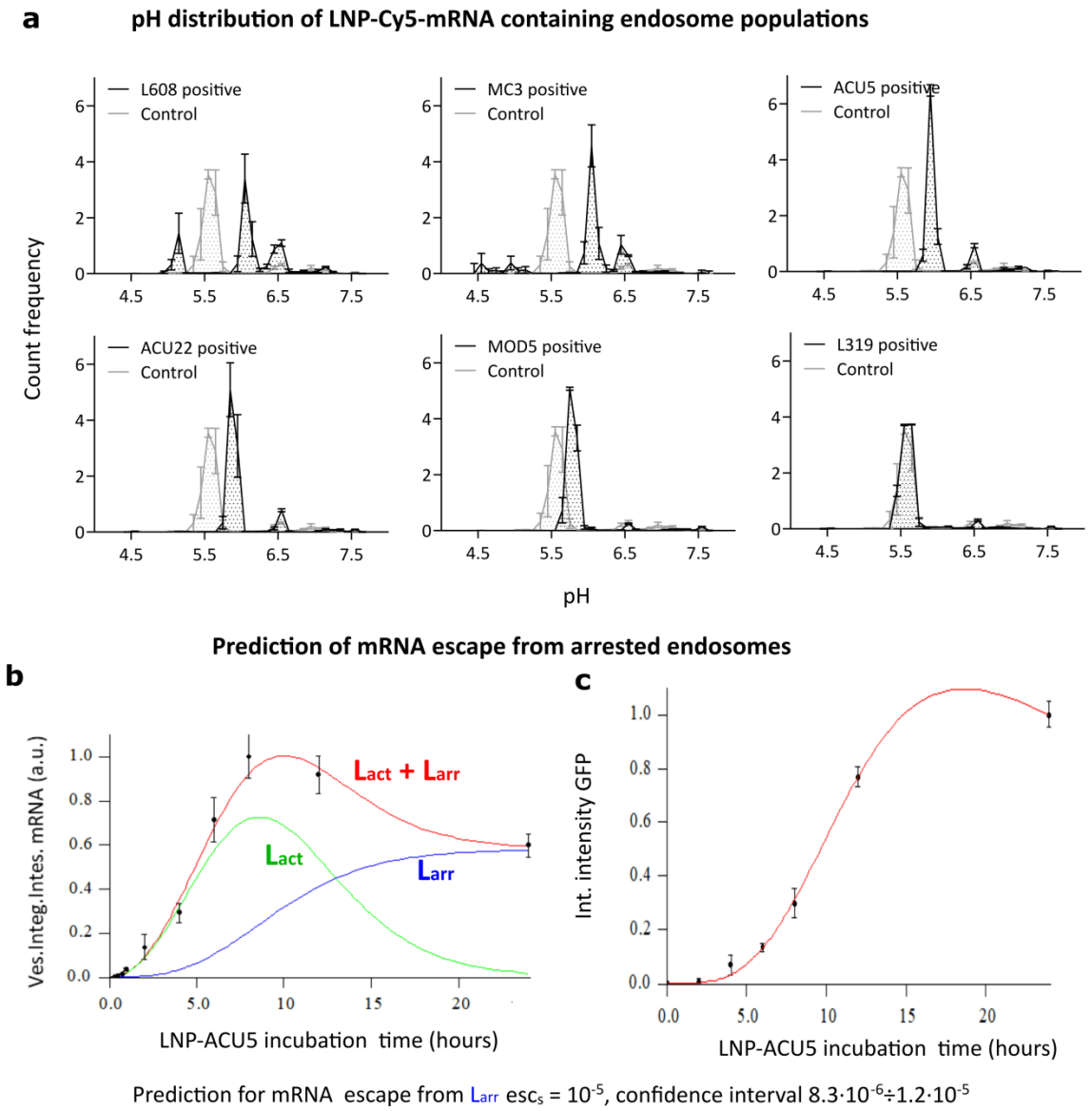

Figure 3: Endosomes accumulating LNP-Cy5-mRNA display acidification defects and negligible endosomal mRNA escape (a) HeLa cells were incubated with pH-sensitive Rodo-Red and pH stable Alexa-488 fluorophore labeled LDLs with and without LNP-Cy5-mRNA, for 2h and imaged live. The pH of LNP-Cy5-mRNA-containing endosomes was calculated by intensity ratiometric analysis from LDL Rodo-Red and LDL-488 (see **Methods**). Whereas in control cells (LDL probes internalized without LNP-Cy5-mRNA, grey line), a significant proportion of endosomes was acidified to pH 5.5, characteristic of late endosomes/lysosomes, most LNP-Cy5-mRNA-containing endosomes (black line) stalled between early (pH 6.5) and late endosomal pH (pH 5.5). **(b-c)** Mathematical model for prediction of mRNA escape from arrested (L_{arr}) endosomes in human primary adipocytes. The theoretical model fit (red lines in panel **b-c**) to experimental ACU5 LNP-Cy5-mRNA uptake kinetics (panel **b**, black dots) and GFP expression (panel **c**, black dots). Green and blue lines denote model predictions for active (L_{act}) and arrested (L_{arr}) endosomes, respectively (see **Methods,** Extended Data Fig. 5a-b). N=3 independent experiments (mean ± s.e.m).

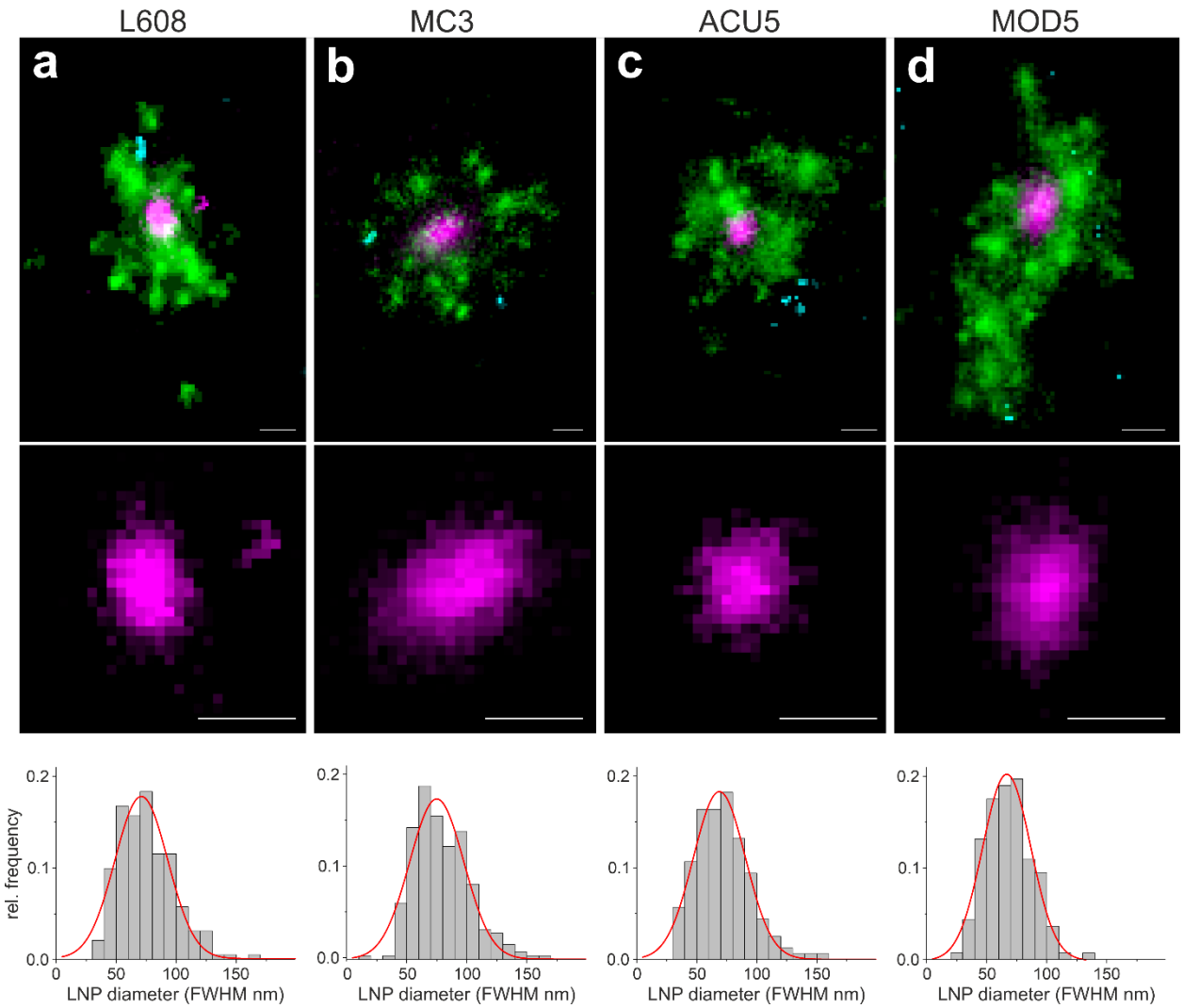

Figure 4. Multi-colour SMLM detects and visualizes singular LNP-mRNA in endosomal compartments with nanometer resolution. **(a-d)** Exemplary images of endosomes containing a single, clearly detectable LNP-mRNA (magenta) together with Transferrin (green) and EGF (cyan) cargo for each imaged LNP formulation (*upper row*). SMLM resolves single LNP as round nano-domains (zoom in, *middle row*) with characteristic size distribution. LNP diameter distributions were built by determining the FWHM of single LNP (see **Methods**). Mean LNP diameters (FWHM) were calculated by Gaussian fitting of the distributions to 74.9 ± 22.6, 71.0 ± 22.0, 66.7 ± 20.2 and 68.9 ± 21.7 nm, respectively (mean ± sd). The cellular context of displayed endosomes is provided in Extended Data Fig. 10, 25, 26-27. Scale bars 100 nm.

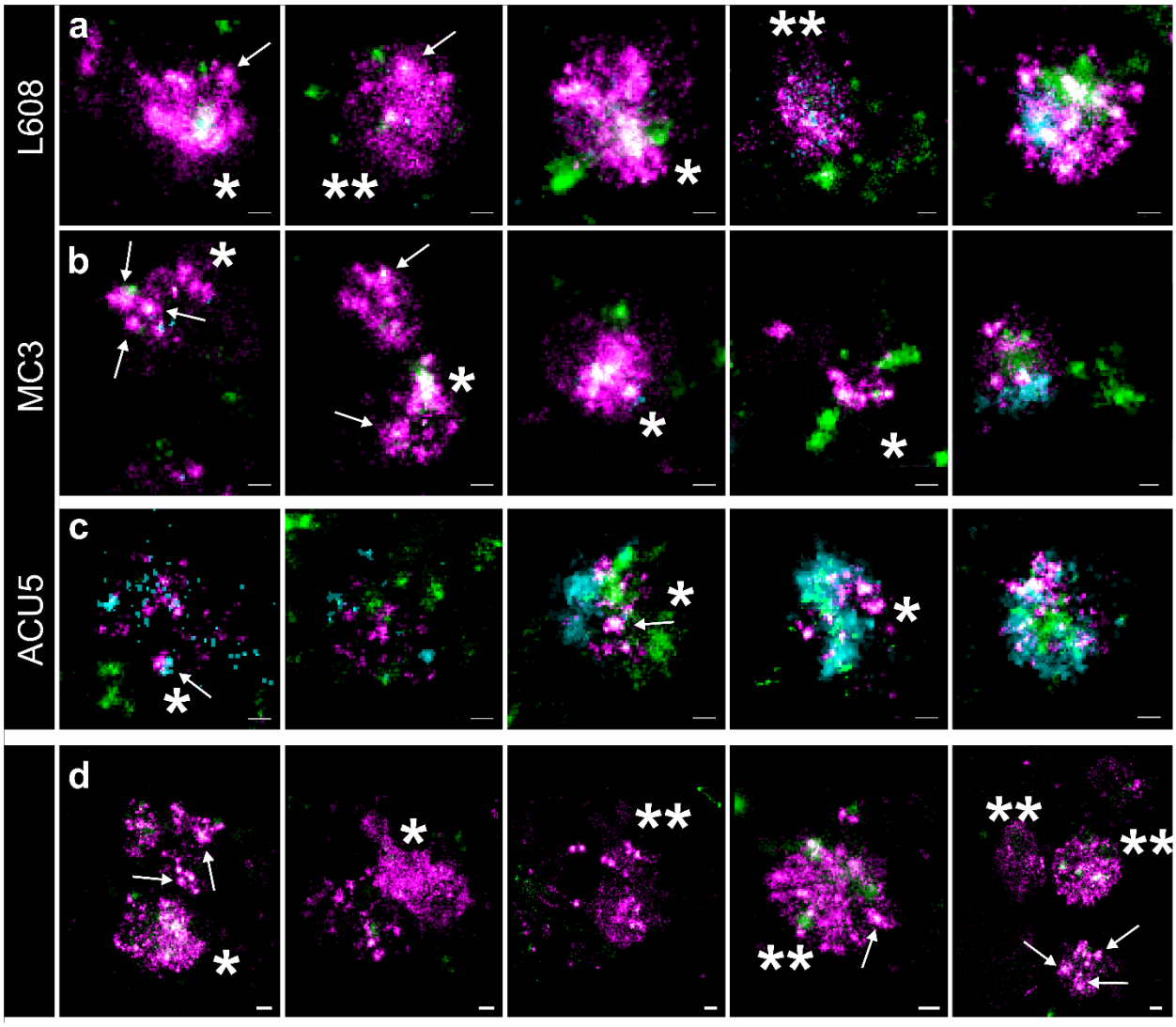

Figure 5. Arrested endosomes are large structures, filled with dense and disperse mRNA and often devoid of endocytosed cargo. (a-c) SMLM visualizes large, LNP-mRNA-rich (magenta) structures in HeLa cells, incubated with L608 (**a**) MC3 (**b**) and ACU5 (**c**) LNP. These endosomes can display an accumulation of LNP-mRNA like puncta (likely to be single LNP indicated with arrows, single asterisk), but more often a disperse signal over large areas (double asterisk). Most endosomes that exhibit these characteristics show a substantial lack of Transferrin (green) and EGF (cyan) cargo compared to endosomes, containing singular LNP (compare Figure 3), although also endosomes with varying degree of cargo-content together with strong mRNA signal can be found (**a,b**: increasing cargo content from left to right). (**c**) In the case of ACU5, large endosomal structures, also containing more than one LNP, can be found. Contrary to **a** and **b**, cells incubated with ACU5 often exhibit endosomes with cargo, especially EGF. (**d)** Arrested endosomes with similar features were consistently found in primary human adipocytes. ROIs, indicating the cellular context of displayed endosomes, are provided in Extended Data Fig. 10-19. Scale bars 100nm.

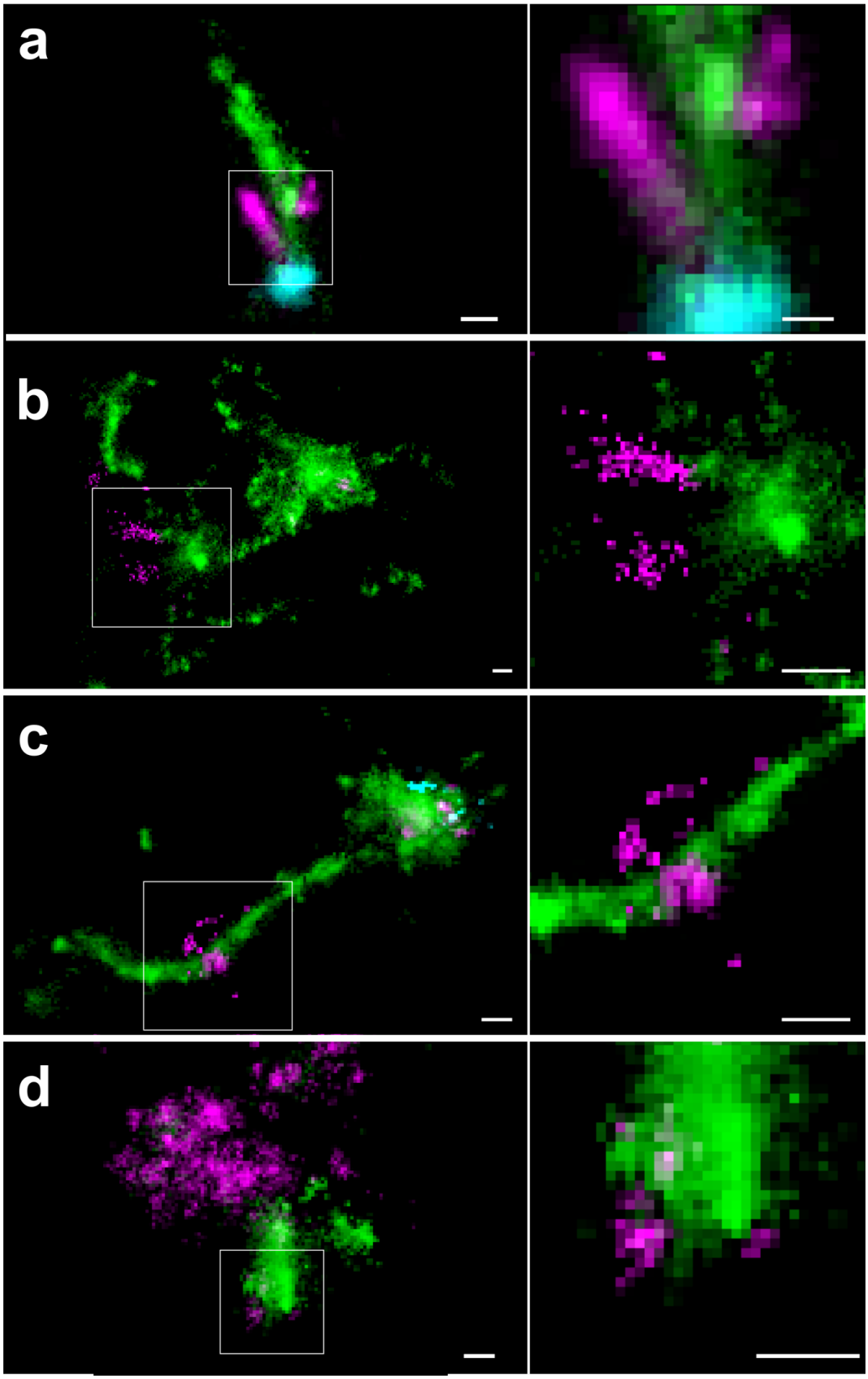

Figure 6. Multi-colour SMLM reveals endosomal mRNA escape at the nanoscale from Transferrin-containing tubules in primary human adipocytes and HeLa cells. Exemplary images of the different observable types of

mRNA (magenta) escape in primary human adipocytes and HeLa cells, related to Transferrin positive tubules (green). **(a)** Concentrated mRNA signal is located at the very tip of a Transferrin positive tubule, connected to an elongated mRNA signal colocalising along the tubule. Very sparse mRNA signal can be detected outside the tubule. **(b)** Disperse mRNA is seemingly emanating from the Transferrin positive tubule, from which it is already segregated. These patterns clearly do not constitute intact LNP and are likely to represent partly stretched mRNA molecules escaping from endosomal structures. **(c)** An LNP is located on a long Transferrin positive tubule, together with a perpendicular disperse mRNA signal, likely representing an instance of mRNA escape. **(d)** In very rare cases, also in arrested endosomes (compare Figure 4), disperse mRNA signal, attached to a Transferrin positive structure, can be detected. ROIs, indicating the cellular context of displayed endosomes, are provided in 15, 17-26. Zoom-in of the indicated regions are presented on the right panels. Scale bars are 100 nm.

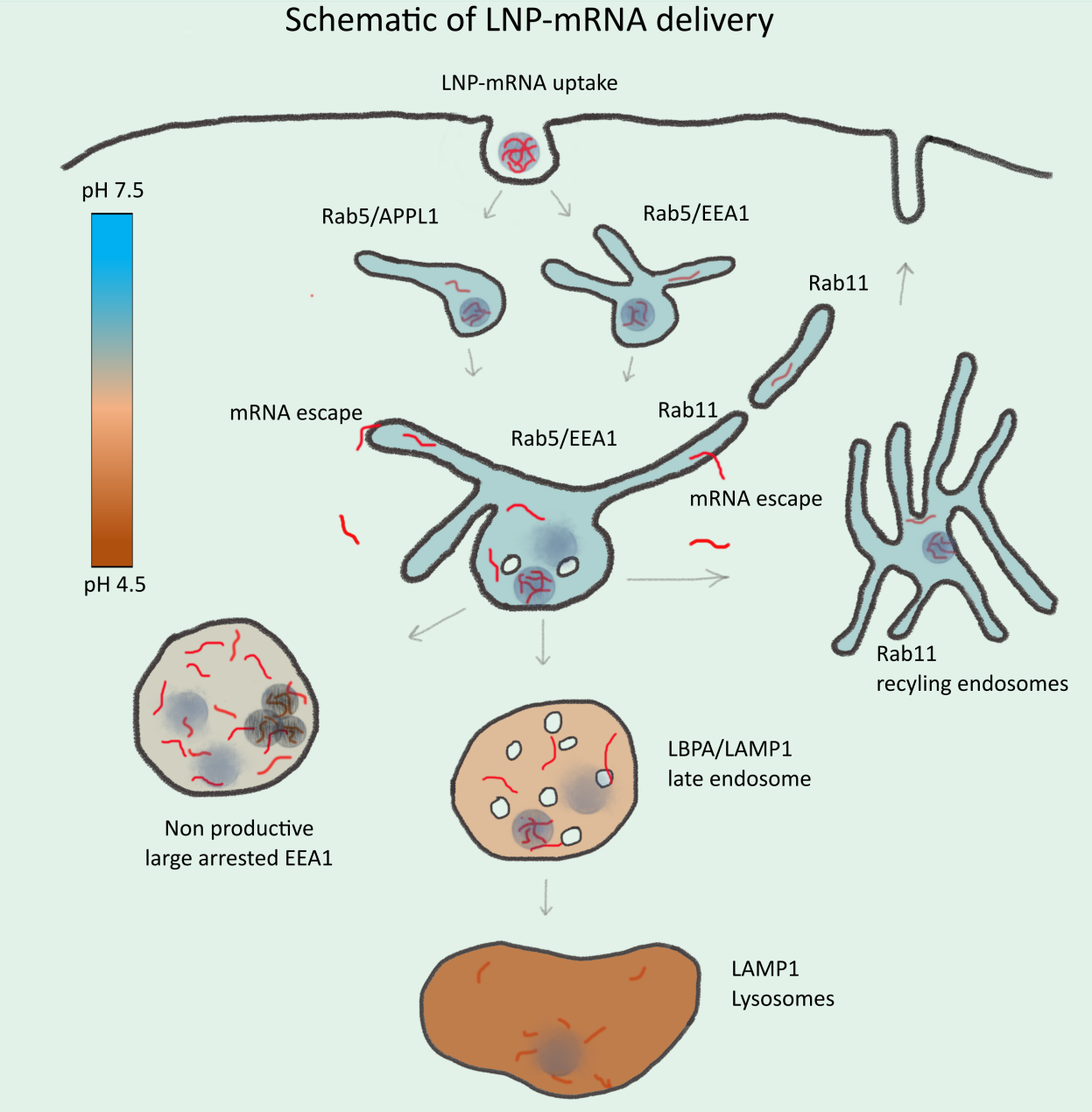

Figure 7: Schematic illustration of endosomal-mediated LNP-mRNA delivery: LNP-mRNA are taken up in cells via endocytosis and sequentially transported to various endosomal compartments. Under normal conditions, these endosomal compartments maintain a characteristic pH (see color heat map) for their functionality. Following uptake, mRNA in endosomes can be detected as individual LNP-mRNA similar to the starting material by SMLM. Acidification of endosomal lumen leads to release of mRNA from LNP and escape from the endosomal lumen into the cytoplasm. Escape occurs mainly from small APPL1-, EEA1- and/or Rab11-positive tubular endosomes. Over time, the majority of LNP-mRNA accumulates in large, EEA1 endosomes where individual compact LNP are disrupted and mRNA signal becomes amorphous. Large endosomes become deficient in acidification, maturation-arrested, and non-productive for delivery. This may account for cytotoxicity of LNP. Late endosomes and lysosomes are not favorable for mRNA escape.